Raman scattering by phonons and magnons in semimagnetic semiconductors: $Cd_{1-x}Mn_xTe$

S. Venugopalan,* A. Petrou, R. R. Galazka,† A. K. Ramdas, and S. Rodriguez
Department of Physics, Purdue University, West Lafayette, Indiana 47907
(Received 28 August 1981)

$Cd_{1-x}Mn_xTe$ alloys possess a homogeneous crystal phase having a zinc-blende structure for $0 \leq x \leq 0.7$. Their Raman spectra exhibit two pairs of sharp lines characteristic of the zone center "CdTe-like" and "MnTe-like" LO-TO modes. Some quasicontinuous features in the Raman spectrum can be traced to first-order processes which become allowed as a result of the absence of strict translational symmetry and reflect the one-phonon density of states. In the antiferromagnetic phase of the alloys ($x > 0.6$) and in the spin-glass phase ($0.17 \leq x \leq 0.6$), a new low-energy Raman line appears. We attribute it to an inelastic scattering involving the emission or absorption of a magnon. The polarization features and the temperature dependence of the magnon line are consistent with this assignment.

I. INTRODUCTION

In semiconductor physics two approaches have been successful in controlling physical properties: (1) impurities intentionally introduced into an otherwise pure host and (2) alloys of two or more well-characterized crystals. The alloys or mixed crystals offer a novel physical system whose properties are of considerable basic interest: electronic band structure, lattice vibrations, and localized electronic and vibrational levels which, in such a system, present unique experimental and theoretical problems. For example, the ternary compound semiconductors formed by HgTe and CdTe exhibit a band gap ranging from zero (HgTe) to ~ 1.6 eV (CdTe); this "tunability" has been exploited in recent years for designing optimized infrared detectors for specific wavelength ranges.[1] It has been appreciated that if an alloy is formed of a II-VI semiconductor (e.g., CdTe) and a magnetic semiconductor (e.g., MnTe), several new physical phenomena arise which can be traced to the magnetic properties of the transition-metal ion.[2–4] These "diluted magnetic semiconductors" or "semimagnetic semiconductors" exhibit g factors for the free carriers which are often in excess of a hundred. In addition they display unusual temperature and magnetic-field dependence. For example, a crystal of $Cd_{0.85}Mn_{0.15}Te$ shows a Faraday rotation[5] of $\sim 10\,000$ deg/cm for a magnetic field of only 5 kG. In $Hg_{1-x}Mn_xTe$, the period and the amplitude of the de Haas–Shubnikov oscillations[6] have been found to undergo large variations even for temperature changes of a few degrees. Galazka *et al.*,[7] have constructed the magnetic phase diagram of $Cd_{1-x}Mn_xTe$ alloys from a study of magnetic susceptibility and specific heat; on going from high to low temperatures, they have discovered the paramagnetic → spin-glass transitions for $0.17 \leq x \leq 0.6$ and paramegnetic → antiferromagnetic transition for $x > 0.6$.

The ability to incorporate a wide range of Mn concentration in $Cd_{1-x}Mn_xTe$ crystals allows one to probe several distinct phenomena as a function of alloy composition. The evolution of phonon spectra in this system, including new impurity-induced effects, is a topic of basic interest in the context of the lattice dynamics of mixed crystals.[8] The band gap of these crystals can be continuously varied[9] from 1.65 eV to 2.3 eV as x ranges from 0.05 to 0.7. The tunability of the gap in the visible region makes these magnetic semiconductors especially attractive for resonance-light-scattering studies using dye lasers. Finally, at sufficiently low temperatures, spin-wave excitations should also be observable in the magnetically ordered phases of these crystals. With these motivations, we have investigated the Raman spectra[10] of this system of diluted magnetic semiconductors. In this paper, we present and discuss the results concerning their phonon and magnon spectra.

II. EXPERIMENTAL

$Cd_{1-x}Mn_xTe$ crystals were grown by a modified Bridgman method. Crystals in the composition range $0.1 \leq x \leq 0.75$ were studied during this investigation. The Mn concentration was established by density, electron microprobe, chemical analysis, and optical-absorption measurements. Pure CdTe samples, both p type and semi-insulating, were also investigated as the limiting case corresponding to $x=0$. X-ray analysis by the Laue method showed that for $x \leq 0.5$ the crystals are cubic and belong to the point group T_d. For $0.5 \leq x \leq 0.7$, the Laue patterns of several samples showed either cubic or uniaxial symmetry. Conceivably, the latter may also arise from twinning effects associated with very small cubic domains and further x-ray studies are needed in order to verify this possibility.[11] With $x > 0.7$, one often obtains an inhomogeneous mixture of different compositions and crystallographic phases, which renders them unsuitable for our experiments.

For polarization studies, the samples were oriented with x-rays and optically polished. They were first ground with successively finer grits of carborundum powder, and then polished on microcloth with 6-μm diamond paste using Metadi oil as lubricant. The final polishing was done on microcloth utilizing a suspension of 0.05-μm alumina powder[12] in distilled water.

Raman spectra were excited with ~ 150 mW of power from a Kr^+ laser (6471, 6764, 7525, or 7993 Å lines) or a dye laser pumped by an Ar^+ laser. Using the dye Rhodamine 590, the dye-laser wavelength could be continuously tuned between 5800 and 6500 Å. The double monochromator and photon-counting system, as well as the experimental procedure used to circumvent the unequal polarization response of the spectrometer, are described elsewhere.[13] When necessary, a triple monochromator was used in order to drastically reduce the stray light. This enabled the observation of weak, low-frequency Raman spectra to within 3 cm^{-1} from the exciting laser line, in spite of the indifferent optical quality of some of the crystals.

The samples were mounted on the cold finger of an optical cryostat. For fixed-temperature measurements down to liquid-helium temperature, a glass cryostat was employed. Variable-temperature measurements over the range 2—300 K were performed using a stainless-steel cryostat[14] and a temperature controller.[15] The sample temperature was measured, to within ± 0.5 K, by a calibrated Si-diode sensor positioned immediately above the copper block on which the sample was mounted. Both right-angle and backscattering geometries were employed. In the latter case, the sample surfaces were polished with Syton[16] just before the measurements; further, whenever necessary, the laser beam was focussed on the surface by a cylindrical lens in order to avoid possible surface damage.

III. RESULTS AND DISCUSSION

In crystals of point group symmetry T_d, Raman scattering arises from excitations which belong to the irreducible representations (Ref. 17) A_1, E, F_2, and F_1. Of these, A_1, E, and F_2 are characterized by symmetric polarizability tensors, whereas the tensors are antisymmetric for F_1. When referred to the three cubic directions ($x||[100]$, $y||[010]$, $z||[001]$) their respective tensors are as follows:

$$A_1: \begin{bmatrix} a & 0 & 0 \\ 0 & a & 0 \\ 0 & 0 & a \end{bmatrix}, \tag{1}$$

$$E: \begin{bmatrix} -b & 0 & 0 \\ 0 & -b & 0 \\ 0 & 0 & 2b \end{bmatrix}, \begin{bmatrix} \sqrt{3}b & 0 & 0 \\ 0 & -\sqrt{3}b & 0 \\ 0 & 0 & 0 \end{bmatrix}, \tag{2}$$

$$F_2: \begin{bmatrix} 0 & 0 & 0 \\ 0 & 0 & d \\ 0 & d & 0 \end{bmatrix} (X), \begin{bmatrix} 0 & 0 & d \\ 0 & 0 & 0 \\ d & 0 & 0 \end{bmatrix} (Y), \begin{bmatrix} 0 & 0 & 0 \\ d & 0 & 0 \\ 0 & p & 0 \end{bmatrix} (Z), \tag{3}$$

$$F_1: \begin{bmatrix} 0 & 0 & 0 \\ 0 & 0 & c \\ 0 & -c & 0 \end{bmatrix}, \begin{bmatrix} 0 & 0 & -c \\ 0 & 0 & 0 \\ c & 0 & 0 \end{bmatrix}, \begin{bmatrix} 0 & c & 0 \\ -c & 0 & 0 \\ 0 & 0 & 0 \end{bmatrix}. \quad (4)$$

It is well known that phonons of F_2 symmetry are infrared active and hence may split into longitudinal-optic (LO) and transverse-optic (TO) components due to the long-range polarization field. In Eq. (3) we have indicated in parentheses the respective phonon polarization associated with each tensor. Antisymmetric Raman scattering by modes of F_1 symmetry is of interest in the context of magnetic excitations, which we shall consider in Sec. III C. In Secs. III A and III B we are concerned with symmetric Raman scattering by phonons, and hence we shall restrict our attention here to modes of A_1, E, and F_2 symmetry.

A. Mixed-crystal phonons

Figure 1 shows the room-temperature spectrum in the 0—220 cm^{-1} range for $x=0.4$. The scattering configuration employed is $y'(z'z')x'$, where x', y', and z' are along [100], [011], and [0$\bar{1}$1], respectively. In this geometry all the zone-center ($\vec{q}\sim 0$) phonons with A_1, E, and F_2 symmetry can be observed. The first-order Raman spectrum of pure CdTe consists[18,19] of a pair of LO-TO lines of F_2 symmetry, which occur at 140 and 171 cm^{-1}, respectively. We note from Fig. 1 that the alloy exhibits a rather intense and quasicontinuous spectrum below 130 cm^{-1}, in addition to the two new lines in the 175—220 cm^{-1} range. This clearly shows that the mixed crystal has a richer and more complex spectrum as compared to that of CdTe.

Polarization features as well as concentration dependence of the spectra provide further insight into their origin. To the extent that the mixed crystal as a whole can be considered to have the point-group symmetry T_d, the spectrum in Fig. 1 can be analyzed in terms of the different Raman-active symmetry species, viz., A_1, E, and F_2. For example, previous studies of Nair and Walker[20] and Harley *et al.*[21] have demonstrated the utility of such an approach in the case of mixed alkali halides. Figures 2 and 3 present (A_1+E), E, F_2(TO), and F_2(LO) spectra for $x=0.4$; indicated in each figure are the symmetry species selected by the respective polarization geometries. From these results we deduce that the two relatively sharp features in Fig. 3(a) at 143 and 189 cm^{-1} are F_2(TO) modes, while those in Fig. 3(b) at 158 and 203 cm^{-1} are F_2(LO) modes. Earlier studies of the vibrational spectra of other II-VI and III-V mixed crystals show that the alloys often display[8] a "two-mode behavior." In such cases, the spectra contain distinct TO and LO modes that can be traced to the individual components of the alloy. Based on the frequencies of the TO and LO lines in CdTe, we identify the lines at 143 and 158 cm^{-1} as the respective TO and LO modes that are characteristic of the CdTe component in the mixed crystal; we refer to them as the "CdTe-like" lines. Similarly, the lines at 189 and 203 cm^{-1} can be regarded as the "MnTe-like" TO and LO modes characteristic of the MnTe component of the alloy.

Figure 4 shows the Raman spectra at 80 K in the range 20—220 cm^{-1} for several alloys. All these spectra were obtained in the right-angle scattering geometry, using a laser wavelength (λ_L) to which the given sample is transparent. However, it should be emphasized that the crystallographic orientation of the samples, as also λ_L, is not identical for these spectra. Hence, due caution should be exercised while making any intercomparisons of the observed features or their intensities in the different spectra. All the same, some qualitative conclusions can be drawn regarding the main features present in each case and their dependence on x. For example, the features in the 20—130 cm^{-1} range become more pronounced with increas-

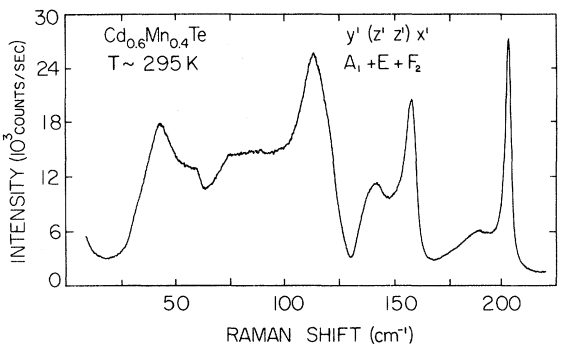

FIG. 1. Raman spectrum of $Cd_{0.6}Mn_{0.4}Te$ at 295 K, excited with 6764-Å Kr^+ laser line. x', y', and z' are along [100], [011], and [0$\bar{1}$1], respectively. The polarization geometry and the allowed phonon symmetries are also indicated.

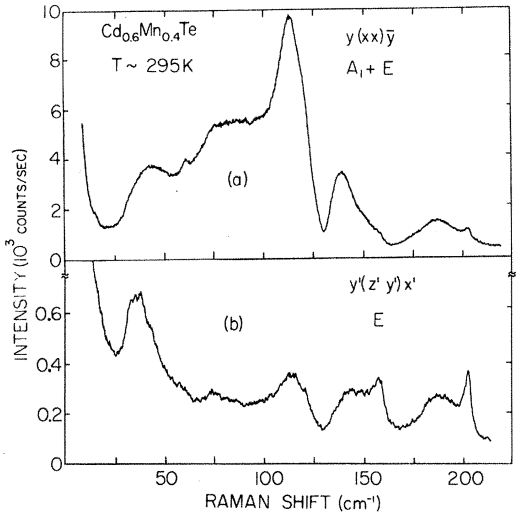

FIG. 2. Polarized Raman spectra of $Cd_{0.6}Mn_{0.4}Te$. (a) $y(xx)\bar{y}$; (b) $y'(z'y')x'$. x, y, and z are along the cubic axes. Other experimental conditions are the same as in Fig. 1.

ing x; also, for larger x the "MnTe-like" modes grow in intensity relative to the "CdTe-like" modes.

The variation of the frequency of these LO and TO modes as a function of x is shown in Fig. 5. It is seen that as $x \rightarrow 0$, the MnTe-like modes merge toward one which can be regarded as the

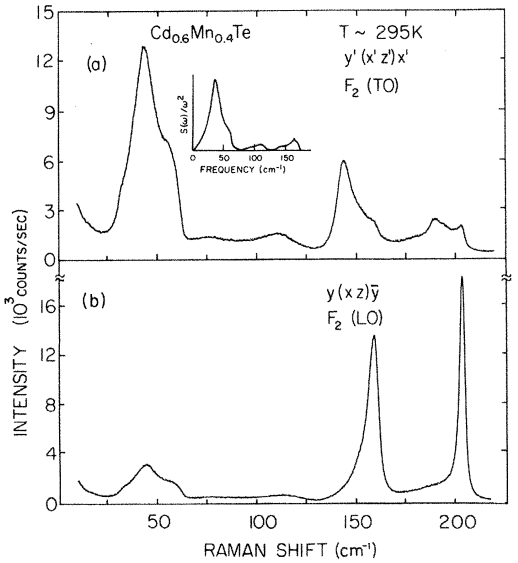

FIG. 3. Polarized Raman spectra of $Cd_{0.6}Mn_{0.4}Te$. (a) $y'(x'z')x'$; (b) $y(xz)\bar{y}$. The significance of the inset in (a) is discussed in the text. The crystallographic axes and other experimental conditions are the same as in Figs. 1 and 2.

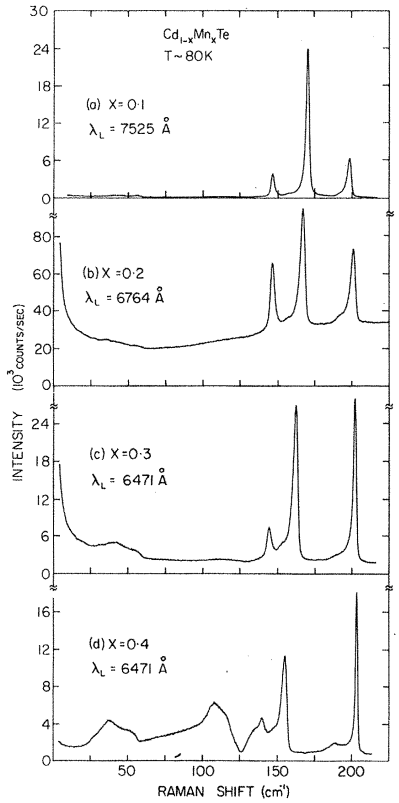

FIG. 4. Raman spectra of $Cd_{1-x}Mn_xTe$ at 80 K. (a) $x = 0.1$; (b) $x = 0.2$; (c) $x = 0.3$; (d) $x = 0.4$. λ_L indicates the exciting laser wavelength used in each case.

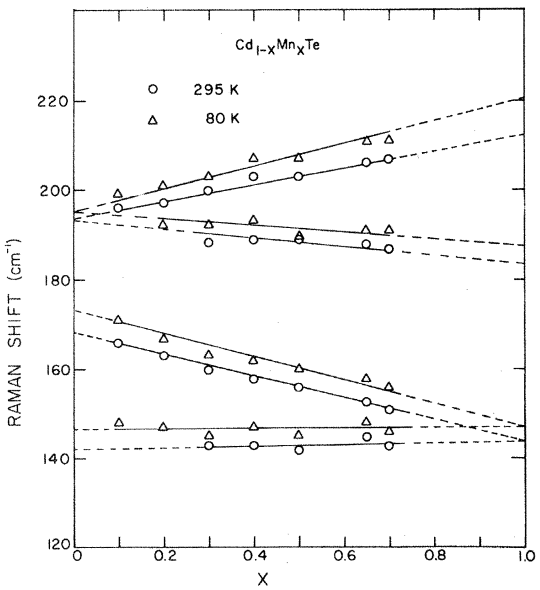

FIG. 5. LO- and TO-mode frequencies in the 140–210 cm^{-1} range as a function of Mn concentration (x). Circles: 295 K; triangles: 80 K.

triply degenerate local mode of Mn in pure CdTe. Similarly, the CdTe-like modes are expected to become degenerate for $x=1$, at which point they must correspond to the gap mode of Cd in the "hypothetical" MnTe crystal[22] with point-group symmetry T_d. The extrapolations shown in Fig. 5 as dashed lines reflect these assumptions. The "two-mode" behavior of the crystals has also been investigated by Picquart *et al.*,[23] from their Raman studies and more indirectly by Gebicki and Nazarewicz[24] through reststrahlen studies; these results are in agreement with ours. In our discussion hereafter, the subscripts 1 and 2 shall denote, respectively, the CdTe-like and the MnTe-like modes.

On the basis of the theory of lattice vibrations of a crystal containing isolated substitutional impurities,[25] one can show that a Mn atom replacing Cd in CdTe will result in a high-frequency local mode and also perhaps a gap mode. On the other hand, Cd in the hypothetical MnTe of a zinc-blende structure can have only the gap mode. The variation of the local mode of Mn in CdTe as a function of x can be calculated at least for small x by considering the mutual interactions of the local modes centered around the different Mn ions. This problem has been discussed by Maradudin and Oitmaa.[26] We give here a simpler approach similar to that used by Fröhlich[27] in the context of the long-wavelength polar modes in an ionic crystal. Consider a crystal of CdTe with a fraction x of the Cd atoms replaced by Mn atoms which are assumed to have charge ze. When the lattice is excited at frequencies near ω_0, the angular frequency of the local mode, the optical modes of the host are quiescent. If $\vec{u}$ is the displacement of the Mn atom in a long-wavelength excitation, we have

$$M'\frac{d^2\vec{u}}{dt^2}=-M'\omega_0^2\vec{u}+ze\vec{E}_l\ , \tag{5}$$

where $\vec{E}_l$ is the local electric field at the position of a Mn ion. We have assumed here that the local mode has an inertia equal to that of the free Mn atom; in any case (z/M') can be viewed as a phenomenological constant. The local electric field $\vec{E}_l$ with the system having uniform polarization $\vec{P}$ is

$$\vec{E}_l=\vec{E}+\frac{4\pi}{3}\vec{P}\ , \tag{6}$$

where $\vec{E}$ is the macroscopic electric field inside the material.

Each Mn ion gives rise to a dipole moment $ze\,\vec{u}$. Since the probability that a cell be occupied by a Mn atom is x, the contribution to the polarization is $(xze\vec{u}/\Omega_0)$, where Ω_0, is the volume of the primitive cell. However, the solid experiences an electronic polarization, which for frequencies below the optical-absorption edge gives rise to a screening of the dipole moments associated with the local modes. This results in a polarization of the medium given by

$$\vec{P}=\frac{xze}{n^2\Omega_0}\vec{u}\ , \tag{7}$$

where n is the index of refraction and $\epsilon_\infty=n^2$ is the so-called high-frequency dielectric constant. Neglecting the effect of retardation, we note that the fields $\vec{E}$, $\vec{P}$, and $\vec{D}=\vec{E}+4\pi\vec{P}$ must obey the equations of electrostatics, i.e., $\vec{\nabla}\cdot\vec{D}=0$ and $\vec{\nabla}\times\vec{E}=0$. In a wave with wave vector $\vec{q}$ these quantities vary as $\exp(i\vec{q}\cdot\vec{r}-i\omega t)$. Thus $\vec{q}\cdot\vec{D}=0$ and, for a longitudinal wave, this yields $\vec{D}=0$, and hence

$$\vec{E}=-4\pi\vec{P}\ . \tag{8}$$

For a transverse wave, on the other hand, $\vec{\nabla}\cdot\vec{E}=-4\pi i\vec{q}\cdot\vec{P}=0$ which , combined with $\vec{\nabla}\times\vec{E}=0$, results in $\vec{E}=0$. Hence, for transverse waves,

$$\vec{E}_l=\frac{4\pi}{3}\vec{P}\ , \tag{9}$$

and for longitudinal waves

$$\vec{E}_l=-\frac{8\pi}{3}\vec{P}\ . \tag{10}$$

Thus, from Eqs. (5), (7), (9), and (10) we find that for transverse (TO) waves

$$\omega_{\rm TO}^2=\omega_0^2-\frac{x}{3}\frac{4\pi z^2e^2}{M'\Omega_0n^2}\ , \tag{11}$$

while for longitudinal (LO) waves

$$\omega_{\rm LO}^2=\omega_0^2+\frac{2x}{3}\frac{4\pi z^2e^2}{M'\Omega_0n^2}\ . \tag{12}$$

For

$$\frac{4\pi z^2e^2}{M'\Omega_0n^2\omega_0^2}<<1\ ,$$

Eqs. (11) and (12) yield

$$\omega_{\rm TO}=\omega_0-\frac{x}{6}\frac{4\pi z^2e^2}{M'\Omega_0n^2\omega_0}\ , \tag{13}$$

$$\omega_{\rm LO}=\omega_0+\frac{x}{3}\frac{4\pi z^2e^2}{M'\Omega_0n^2\omega_0}\ , \tag{14}$$

respectively.

Equations (13) and (14) give the frequencies of the additional modes arising from alloying as x increases; for $x=1$ these modes become the long-wavelength transverse and longitudinal optical-mode frequencies of cubic MnTe. Conversely, the TO and LO modes of CdTe change with increasing x and become eventually the gap mode of Cd impurity in cubic MnTe. The variation of ω_{TO} and ω_{LO} with x need not be linear since the index of refraction n as well as z and conceivably M' can be functions of x. In view of the approximations and assumptions involved in deriving Eqs. (13) and (14) there is no reason to expect the observed linear dependence on x exhibited within experimental errors by the CdTe-like and the MnTe-like modes. It is interesting to note that the slopes of the lines for $\omega_{TO}(x)$ and $\omega_{LO}(x)$ have the expected sign and order of magnitude. An order of magnitude estimate gives

$$\omega_0=\omega_{TO}(\mathrm{CdTe})[1+(M'-M)/M]^{-1/2},$$

which for Mn in CdTe gives $\omega_0\approx 1.43\omega_{TO}(\mathrm{CdTe})$ or 200 cm^{-1} which is to be compared with the room-temperature experimental value of 194 cm^{-1}. Using $n^2=6.4$, $z=2$, and $a=6.48$ Å as the lattice constant of CdTe,[28] Eq. (13) and Eq. (14), we obtain -0.034 and 0.069 for the slopes of $(\omega_{TO}-\omega_0)/\omega_0$ and $(\omega_{LO}-\omega_0)/\omega_0$ as functions of x, respectively; these are to be compared with -0.05 and 0.10, the corresponding room-temperature values for the "MnTe-like" TO and LO modes. For the gap mode and hence for the "CdTe-like" modes, qualitatively similar behavior is expected, though the simple results embodied in Eqs. (13) and (14) need not be accurate in view of the proximity of the frequencies of other lattice vibrations.

The variation of the LO- and TO-mode frequencies with alloy composition was considered also by Picquart *et al.*,[23] in terms of the random-element isodisplacement model. Using four adjustable parameters, they have generated theoretical curves which are in agreement with the experimental data. Barker and Sievers[8] have discussed the different criteria proposed in earlier studies to explain the mode behavior in mixed crystals. More recently, Jahne[29] has pointed out that two-mode behavior can occur in mixed crystals of the type $A_{1-x}BC_x$, only if there exists a gap between the optical-phonon density of states of the two end members AC and BC. From the extrapolations indicated in Fig. 5 at $x=1$ and $x=0$, it appears that Jahne's criterion is satisfied by CdTe and the "hypothetical" MnTe crystal with a zinc-blende structure. Here we draw attention to the paper by Genzel, Martin, and Perry[30] in which a detailed treatment of the zone-center optical phonons using the local electric field defined by the macroscopic parameters of the end members is given. They have illustrated the success of their model in a wide variety of $AB_{1-x}C_x$ alloys exhibiting "two-mode" as well as other patterns of behavior.

When the heavier Cd atom is replaced by Mn, one expects that below the TO-mode frequency of CdTe there should appear new features corresponding to band modes. This is borne out by the pronounced low-frequency modes seen in Figs. 1–4 in the 20–130 cm^{-1} range. These features persist over the composition range $x=0.4-0.7$, but are considerably weaker for $x\leq 0.3$. Also, for any given x, the higher the sample temperature the greater is their intensity. The presence of Mn at random sites within the lattice effectively destroys the translational periodicity in the mixed crystals. Thus, although only zone-center ($\vec{q}\sim 0$) optical phonons are allowed in the first-order Raman spectrum of a perfect crystal, the $\vec{q}\sim 0$ selection rule is relaxed in the alloys. Consequently, they may exhibit one-phonon Raman scattering due to optic and acoustic phonons with all possible $\vec{q}$ vectors spanning the Brillouin zone. As a substitutional impurity, Mn retains the site symmetry T_d in the mixed crystal. Hence, the new impurity-induced features of the spectrum should again belong to the Raman-active representations[31] of T_d, viz., A_1, E, and F_2.

Figures 2 and 3 display the striking polarization behavior of these low-frequency modes. The asymmetric peak centered at 42 cm^{-1} in Fig. 3(a) exhibits a predominant polarization characteristic of transverse F_2 modes. While investigating the side-band absorption associated with the local mode of Be in CdTe, Sennett *et al.*,[32] performed a shell-model calculation of the weighted density of one-phonon states, $S(\omega)/\omega^2$, for CdTe. We note that in the 20–130 cm^{-1} range the main features of Fig. 3(a) bear a striking similarity to their calculated function $S(\omega)/\omega^2$, shown as an inset in the same figure. The one-phonon density of states in CdTe has also been determined experimentally by Rowe *et al.*[33] using neutron inelastic scattering. Their results reveal a prominent peak at ~ 40 cm^{-1} due to transverse-acoustic (TA) phonons and a less intense peak at ~ 110 cm^{-1} due to longitudinal-acoustic (LA) phonons. Furthermore,

their comparison of the frequency distributions of CdTe and InSb shows that as compared to InSb, the optic and LA modes of CdTe show a clear "softening," but the TA modes lie closely within the same range of frequencies for both compounds. We therefore conclude that the peak in Fig. 3(a) at 42 cm^{-1} originates due to disorder-activated, first-order Raman scattering by TA phonons and that it reflects the corresponding TA-phonon density of states in the mixed crystal.

A similar peak due to LA phonons is expected and this may well be the relatively weak peak seen at ~ 110 cm^{-1} in Fig. 3. However, we note from Fig. 2 that there is an intense feature of A_1 symmetry at 112 cm^{-1} and a "spill-over" of its intensity in a forbidden polarization may also contribute to the intensity of the F_2 spectra near 110 cm^{-1}.

The A_1 mode at 112 cm^{-1} exhibits a peculiar line shape suggestive of a Fano-type interference[34] between a discrete mode and an overlapping continuum of states in the same region. There is a distinct possiblity that the discrete level is associated with the breathing mode of nearest-neighbor Te atoms around an impurity atom (Mn or Cd) which remains immobile.[31] In such a case, the frequency of the mode would be *independent* of the mass of the impurity atom, but determined solely by its interactions with the nearest-neighbor Te atoms. If we assume that the relevant force constants are identical for Cd-Te and Mn-Te pairs, the A_1-mode frequency would be a characteristic feature of the mixed crystal, and largely insensitive to the alloy composition. Our observations over the range $x=0.3-0.7$ confirm that the peak position does remain unaffected by the alloy composition over this range. It is also interesting to mention here that a very similar feature of comparable line shape is seen[35] in the Raman spectrum of $Cd_{1-x}Mg_xTe$ at 118.8 cm^{-1}. This frequency is surprisingly close to what we observe in $Cd_{1-x}Mn_xTe$, although the atomic mass of Mn is nearly twice that of Mg. This provides added support to our assignment of the origin of the A_1 mode in Fig. 2(a). Further experiments are planned to characterize its behavior under hydrostatic stress and establish the exact origin of its line shape. We emphasize, however, that the A_1 mode described above is activated by substitutional impurities, and it is not a zone-center phonon of the perfect crystal with zinc-blende structure.

Only modes of E symmetry are allowed in the $y'(z'y')x'$ configuration. Figure 2(b) shows that the intensity of this spectrum is almost 2 orders of magnitude smaller than those which appear in Fig. 1. Moreover, the very weak features manifested in this spectrum appear with maximum intensity in the spectra corresponding to A_1 and F_2 symmetries and could well be due to "spill-over" of their intensities in this spectrum. Thus our results indicate the absence of any intense feature of E symmetry in the spectra.

In the room-temperature spectra of samples with $x \geq 0.1$, we have observed additional, broad Raman lines in the 210—420 cm^{-1} region. Figure 6 shows these lines for $x=0.4$ Their intensity is nearly 2 orders of magnitude lower than those observed in the range below 210 cm^{-1}. These weaker lines practically disappear when the sample is cooled to 80 K. They occur in a spectral range where two-phonon processes involving overtones and combinations can be observed. Tentatively, we assign the following features to the respective overtones and combinations given in parentheses: 293 cm^{-1} ($2TO_1$), 322 cm^{-1} ($2LO_1$), 343 cm^{-1} (TO_1+TO_2), 363 cm^{-1} (LO_1+LO_2), and 401 cm^{-1} ($2LO_2$).

From extended spectral scans at 300 K up to a shift of 3000 cm^{-1}, we ascertained that the alloys possess no other phonon Raman lines at higher frequencies.

B. Resonant and forbidden scattering effects

It is well known that a resonant enhancement of the Raman scattering intensities should occur whenever the energies of the incident ($\hbar\omega_L$) or scattered photons ($\hbar\omega_S$) lie close to the energy of an electronic excitation of the medium. In the case of polar semiconductors, the dependence of the Raman intensities on $\hbar\omega_L$ exhibits several additional features in the vicinity of the fundamental energy gap (E_g) of the crystal; very striking effects due to resonant cancellation, multiple LO-phonon scatter-

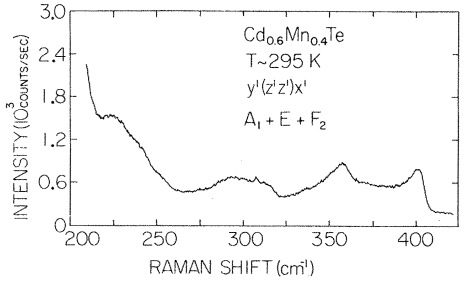

FIG. 6. Raman spectrum of $Cd_{0.6}Mn_{0.4}Te$ in the 210—420 cm^{-1} range. The experimental conditions are the same as in Fig. 1.

ing as well as forbidden one-LO phonon scattering have been observed,[36–38] for example, in CdS and GaAs. Studies of these effects provide valuable insight into the different mechanisms of the scattering process; in addition, they are helpful in characterizing the intermediate electronic states which participate in the scattering process.

We have investigated both one-phonon and multiphonon resonant scattering in these mixed crystals, for $0 \leq x \leq 0.3$. Figure 7 shows the results obtained at 80 K for $x = 0.1$ in the two-mode region. Traces (a) and (b) were taken in the backscattering geometry for $\vec{q} \| [110]$; here $\vec{k}_i$ and $\vec{k}_s$ denote the wave vectors of the incident and scattered photons, respectively. Trace (c) corresponds to the right-angle scattering geometry $y'(x'z')x'$

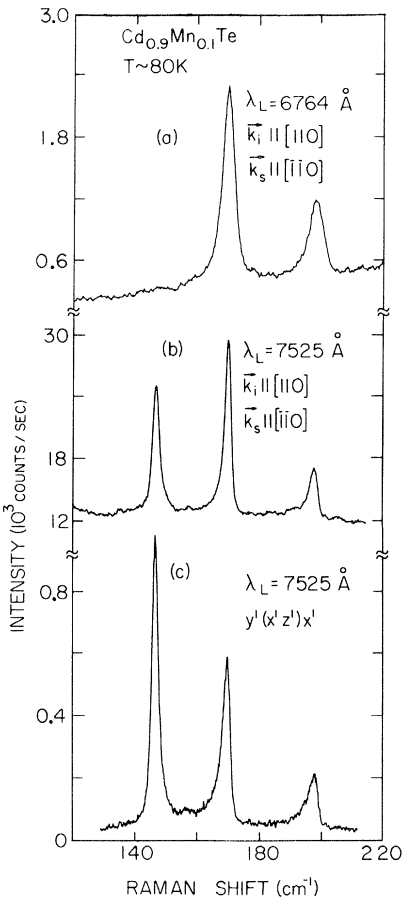

FIG. 7. Forbidden LO- and allowed TO-phonon scattering in $Cd_{0.9}Mn_{0.1}Te$. $T \sim 80$ K; (a) Backscattering along [110] with $\lambda_L = 6764$ Å. (b) Backscattering along [110] with $\lambda_L = 7525$ Å. (c) Right-angle scattering in the $y'(x'z')x'$ geometry, as in the case of Fig. 3(a), with $\lambda_L = 7525$ Å. Note $\vec{k}_i$ and $\vec{k}_s$ denote the wave vectors of the incident and scattered photons, respectively.

which is identical to that used in Fig. 3(a). The respective λ_L is indicated for each spectrum. In all three spectra, the TO phonons are allowed, whereas the LO phonons are forbidden according to the usual polarization selection rules. In contrast to these predictions, we observe the LO phonons very clearly in both scattering geometries and for both λ_L's. The CdTe-like TO phonon is extremely weak for $\hbar\omega_L > E_g$(1.72 eV) as seen in Fig. 7(a). On the other hand, this line appears quite strongly in traces (b) and (c) where $\hbar\omega_L < E_g$, but quite close to the band gap.

Forbidden and resonant one-LO-phonon scattering has been reported earlier in other semiconductors for exciting radiation energies above as well as below E_g. It was shown[36,37] that (i) $\vec{q}$-dependent, intraband Fröhlich interactions, (ii) $\vec{q}$-independent, impurity-induced effects, and (iii) surface electric fields at the depletion layer are the three main processes, in general, that can cause forbidden LO scattering. The resonance of the allowed TO modes, on the other hand, can be readily understood on the basis of the deformation-potential interaction.[37] We believe that the forbidden LO scattering seen in Fig. 7 could be dominated by the possible presence of impurities in our sample. Further experiments which test the $\vec{q}$ dependence of this scattering are essential in order to ascertain the relative contribution from intraband Fröhlich interaction.

The ratio of the intensities of the CdTe-like TO and LO modes (I_{TO}/I_{LO}) shows a marked dependence on the exciting wavelength, as is evident from traces (a) and (b). With $\lambda_L = 7993$ Å this ratio decreased by a factor of 3, when compared to $\lambda_L = 7525$ Å. Selders *et al.*,[19] also observed a simi lar decrease in CdTe when $\hbar\omega_L$ was tuned away from E_g towards lower energies.

In order to study the resonance effects in the vicinity of E_g as a function of λ_L, we investigated a $x = 0.3$ sample at 80 K using dye-laser excitation. At this temperature E_g is ~ 2.012 eV for this alloy. The backscattering geometry was used with $\vec{q} \| [110]$. In Fig. 8 traces (a), (b), and (c) correspond, respectively, to $\hbar\omega_L > E_g$, $\hbar\omega_L \sim E_g$ and $\hbar\omega_L < E_g$. The exciting laser power is also indicated for each spectrum. All three spectra present clear evidence of forbidden scattering from both LO modes. The allowed TO modes are seen in traces (b) and (c), but they practically disappear when $\hbar\omega_L > E_g$. As in the case of CdTe, we again find that the LO peaks are more intense for $\vec{E}_i \| \vec{E}_s$ than with $\vec{E}_i \perp \vec{E}_s$. The sloping background in the

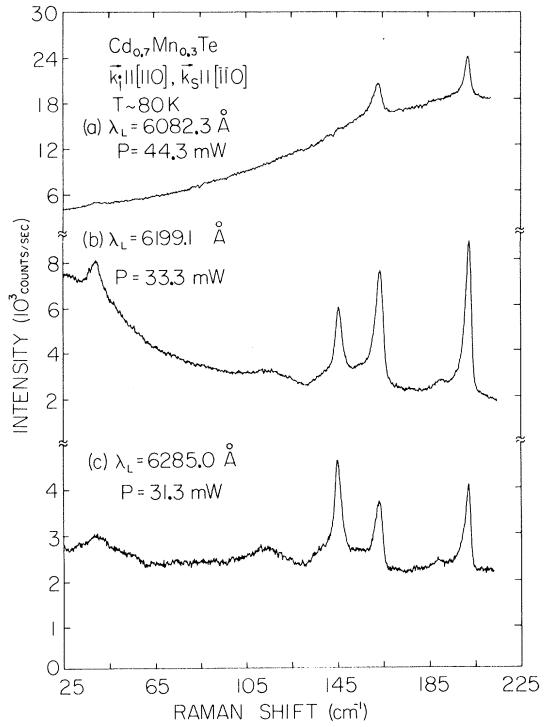

FIG. 8. Resonant and forbidden scattering effects in $Cd_{0.7}Mn_{0.3}Te$ as a function of the dye-laser wavelength. $T \sim 80$ K; $\vec{k}_i \| [110]$, $\vec{k}_s \| [\bar{1}\bar{1}0]$. The laser power used and λ_L are indicated for each spectrum.

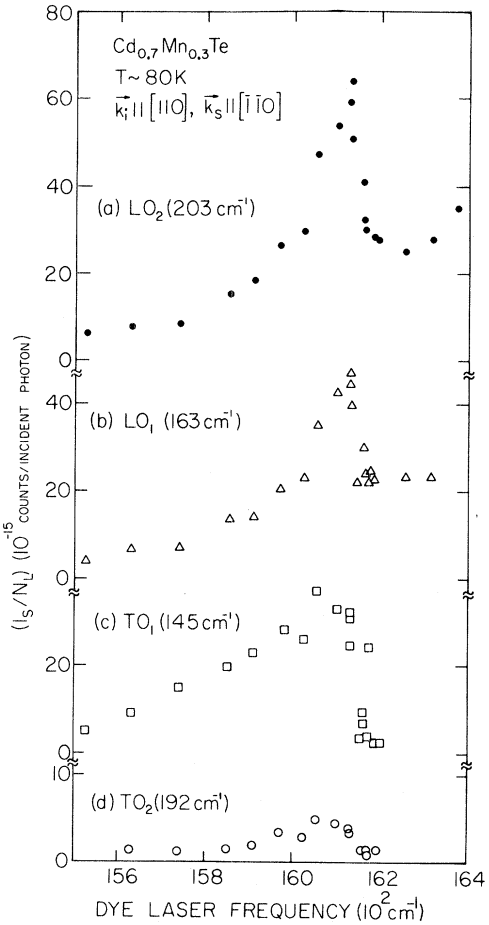

FIG. 9. Normalized intensity (I_s/N_L) of the LO and TO modes of $Cd_{0.7}Mn_{0.3}Te$, as a function of the dye-laser frequency in the vicinity of E_g. The experimental conditions are those of Fig. 8.

top two spectra is due to a broad luminescence emission of the sample. The intensity (I_S) of the TO and LO modes, normalized to the number of incident laser photons (N_L), is plotted in Fig. 9 as a function of the dye-laser frequency. These data are uncorrected for the absorption in the sample close to and above E_g. This would distort the resonance profiles shown here, especially for $\hbar\omega_L > E_g$. Even so, our data demonstrate the resonant increase in the intensity of the forbidden LO as well as allowed TO modes as $\hbar\omega_L$ approaches E_g from below. Further, we note that the TO modes disappear rather abruptly when $\hbar\omega_L$ exceeds E_g, but this is not true of the LO modes. This again implies that the scattering mechanisms are not identical for the two types of modes. As mentioned earlier, we believe that impurity effects are largely responsible for the forbidden LO scattering seen here.

In Fig. 8(b), a low-frequency mode is seen to emerge at 40 cm^{-1}. This line is most intense under resonance conditions, and it progressively disappears as λ_L is tuned away from resonance on either side. We ascribe it to the difference LO-phonon mode, i.e., ($LO_2 - LO_1$), which is normally expected to be extremely weak at 80 K. This is due to the rather small value of the Bose-Einstein factor,

$$n_0 = 1/(e^{\hbar\Omega/k_B T} - 1) \approx 0.05 , \qquad (15)$$

where $\hbar\Omega$ is the energy of the LO_1 phonon. It is therefore understandable that at low temperatures, such a mode would appear only under conditions of resonant enhancement. On the other hand, one expects to see this mode more easily at 300 K. Accordingly, we investigated the $x = 0.2$ and 0.3 samples in the backscattering geometry using $\lambda_L = 6764$ Å. These results are shown in Fig. 10. Trace (a) was obtained using an arbitrary sample surface whose normal was not along any of the crystallographic symmetry axes, whereas we used a (110) face for trace (b). Also for trace (b), $\hbar\omega_L$ lies just below E_g, while for the former $\hbar\omega_L > E_g$. In both cases we observe a low-frequency mode whose

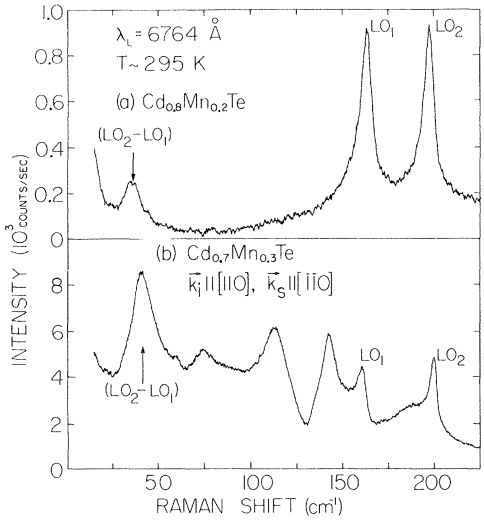

FIG. 10. Difference LO-frequency modes seen in the backscattering geometry at 295 K; $\lambda_L = 6764$Å. (a) $x = 0.2$; the normal to the sample surface is not along a crystallographic symmetry axis. (b) $x = 0.3$; $\vec{k}_i \| [110]$, $\vec{k}_s \| [\bar{1}\bar{1}0]$.

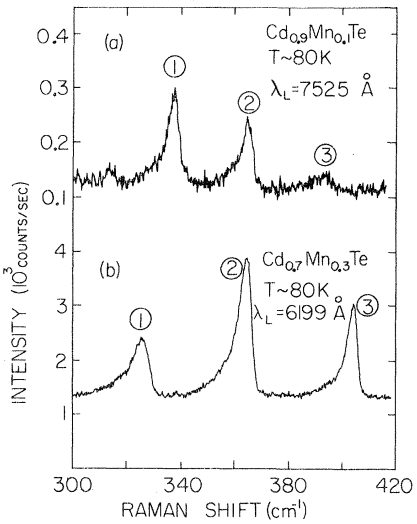

FIG. 11. Overtones and sum of the LO modes observed for (a) $x = 0.1$ and (b) $x = 0.3$. $T \sim 80$ K. The respective λ_L is indicated for each spectrum. The labels 1, 2, and 3 denote peaks corresponding to 2 LO_1, $LO_1 + LO_2$, and 2 LO_2 respectively.

position exactly matches $LO_2 - LO_1$. From Fig. 5, this difference frequency mode is expected to occur at a higher frequency for $x = 0.3$ as compared to $x = 0.2$. This is clearly borne out by our results: The respective peaks occur at 40 and 34 cm^{-1}. These are superimposed on the weaker peaks due to the TA-phonon density of states which fall in the same region. However, the difference LO modes disappear at low temperatures as they also do away from resonance, as seen from Figs. 4 and 8(c).

We have also observed a resonant increase of the intensity of overtones and sum of the LO modes, i.e., $2LO_1$, $(LO_1 + LO_2)$, and $2LO_2$ as $\hbar\omega_L$ approaches E_g. Typical spectra are shown in Fig. 11 for $x = 0.1$ and $x = 0.3$. Dye-laser excitation was employed in the latter case. For $x = 0.1$, the $2LO_2$ mode is much weaker than $2LO_1$. Understandably, this is due to the low Mn concentration of this alloy.

C. Magnetic excitations

The specific-heat and magnetic-susceptibility studies of Galazka *et al.*[7] show that below T_N, a temperature characteristic of any given x, $Cd_{1-x}Mn_xTe$ crystals become antiferromagnetic for $x > 0.6$ and spin-glass for $0.17 \leq x \leq 0.6$. We have investigated the Raman scattering associated with the magnetic excitations in the antiferromagnetic, spin-glass, as well as the paramagnetic, phase. Such excitations can be characterized by a magnetization of the medium, $\vec{M}(\vec{r},t)$ which can be expanded in a Fourier series as

$$\vec{M}(\vec{r},t) = \sum_{q} \vec{M}(\vec{q}) \exp[i(\vec{q}\cdot\vec{r} - \omega_q t)] + \text{c.c.} \tag{16}$$

The quantized magnetic excitations are the magnons. The low-temperature phases exhibit order caused by an exchange interaction between the spins of Mn^{2+}. For developing a simple picture we consider an antiferromagnetic phase which at $T = 0$ K has equal numbers of Mn^{2+} spins parallel and antiparallel to a preferred direction established by a magnetic field $\vec{H}_A$ introduced phenomenologically and referred to as the anisotropy field. Within the framework of a molecular-field theory the net magnetization is a superposition of two interpenetrating magnetizations, $\vec{M}_1$ and $\vec{M}_2$ preferentially parallel and antiparallel to $\vec{H}_A$, respectively. In addition a Mn^{2+} ion in set 1 (2), experiences an exchange field $-\lambda\vec{M}_2$ $(-\lambda\vec{M}_1)$. In equilibrium the net magnetization $\vec{M} = \vec{M}_1 + \vec{M}_2$ is zero. Magnetic excitation corresponding to the Fourier components in Eq. (16) can be produced thermally, or by interaction with electromagnetic radiation

which is either absorbed (infrared absorption) or inelastically scattered (Raman scattering). The induced polarization $\vec{P}$ under the influence of a monochromatic laser radiation of frequency ω_L incident on the crystal is

$$\vec{P}=\chi(\vec{M})\cdot\vec{E}_L \ , \tag{17}$$

where χ is the electric susceptibility, a functional of $\vec{M}$, and $\vec{E}_L$ the electric field of the incident radiation. The modulation of $\vec{P}$ resulting from magnetic excitations is obtained from a Taylor-series expansion of the functional $\chi(\vec{M})$. We write $\vec{P}=\vec{P}^{(0)}+\vec{P}^{(1)}+\vec{P}^{(2)}+\cdots$, where the superindex denotes the number of magnetic excitations involved. The restrictions imposed by the Onsager reciprocity relation, the lack of absorption in the frequency region under consideration, and the crystal symmetry require that[39]

$$\vec{P}^{(1)}=iG\vec{M}\times\vec{E}_L \ , \tag{18}$$

where G is a constant. It is not necessary to consider the spatial variation of $\vec{M}$ because of the wave-vector selection rule as applied to light scattering with a single magnon. The scattering cross section σ for Raman scattering involving one magnon is proportional to $(\hat{\epsilon}_s\cdot d^2\vec{P}/dt^2)^2$, where $\hat{\epsilon}_s$ is the polarization of the scattered radiation. Thus

$$\sigma\propto[(\hat{\epsilon}_s\times\hat{\epsilon}_L)\cdot\vec{M}]^2 \ , \tag{19}$$

where $\hat{\epsilon}_L$ is the polarization of the incident radiation. For the second-order Raman scattering, involving, e.g., the emission of two magnetic excitations, we obtain terms quadratic in the Fourier components in Eq. (16). Thus, the scattering cross section contains, in addition to other contributions, terms proportional to $\hat{\epsilon}_s\cdot\hat{\epsilon}_L\ \vec{M}(\vec{q})\cdot\vec{M}(-\vec{q})$ and $(\hat{\epsilon}_s\times\hat{\epsilon}_L)\cdot[\vec{M}(\vec{q})\times\vec{M}(-\vec{q})]$. This implies that, while the inelastic scattering with a single excitation is antisymmetric, that involving two such excitations is characterized by both symmetric and antisymmetric components of the polarizability tensor.[40]

Figure 12(a) shows the Raman spectrum of the $x=0.7$ sample at 295 K. The sample was an unoriented single crystal in the form of a parallelepiped with optically polished faces. The interpretation of the different phonon features seen here has already been discussed in Sec. III A. Below T_N ($\sim$36 K) the sample must transform from the paramagnetic to the antiferromagnetic phase[7]; in the latter there is antiparallel ordering of adjacent Mn^{2+} spin moments. Figure 12(b) shows that on cooling to 5 K a very distinct Raman line

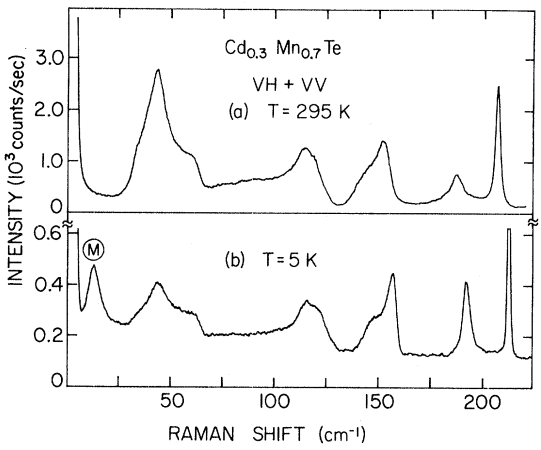

FIG. 12. Raman spectra of $Cd_{0.3}Mn_{0.7}Te$ in the paramagnetic and antiferromagnetic phases; $\lambda_L=6764$ Å. The phase transition occurs (Ref. 7) at $T_N\sim36$ K. The scattering geometry corresponds to $VH+VV$. (a) $T=295$ K and (b) $T=5$ K. M denotes the peak due to magnon scattering.

emerges at 12.5 cm^{-1}, its intensity being comparable to the other spectral features associated with phonons. Both the Stokes as well as the anti-Stokes lines associated with this excitation are clearly observable; further confirmation that it is a Raman line was obtained by using other exciting laser lines. Based on its temperature dependence and polarization behavior, as discussed below, we assign this new low-frequency line to scattering by magnons in the antiferromagnetic phase.

Figure 13 shows that the frequency and the intensity of this line decrease markedly with increasing temperature and the line finally disappears above T_N. This behavior clearly indicates that the origin of this line is associated with the magnetic ordering in the antiferromagnetic phase. In the following discussion, the scattering plane is horizontal and the incident radiation is vertically polarized; we designate the geometry where the scattered radiation is analyzed along the horizontal direction as VH and that analyzed along the vertical as VV. As discussed above, the Raman tensor characterizing a one-magnon scattering process exhibits antisymmetric behavior.[40,41] Thus, the scattering must vanish for any diagonal component of the Raman tensor, such as in the VV spectrum, irrespective of the crystallographic orientation of the sample. We find that the line at 12.5 cm^{-1} appears only in those geometries where the incoming and the scattered photons are polarized perpendicular to each other, as in the VH spectrum; on the

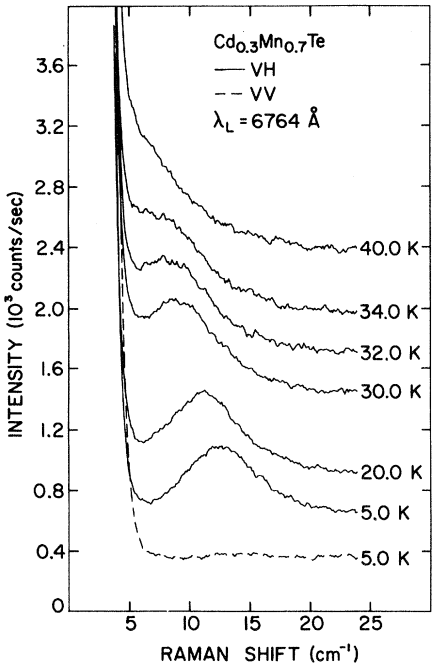

FIG. 13. Temperature dependence of the low-frequency Raman spectrum of $Cd_{0.3}Mn_{0.7}Te$. The intensity scale refers to the *VV* spectrum at 5 K and successive spectra have been displaced vertically upwards for clarity. The sample temperature is indicated for each trace. The broken curve shows the *VV* spectrum. All the other spectra correspond to *VH* polarization. λ_L indicates the exciting laser wavelength.

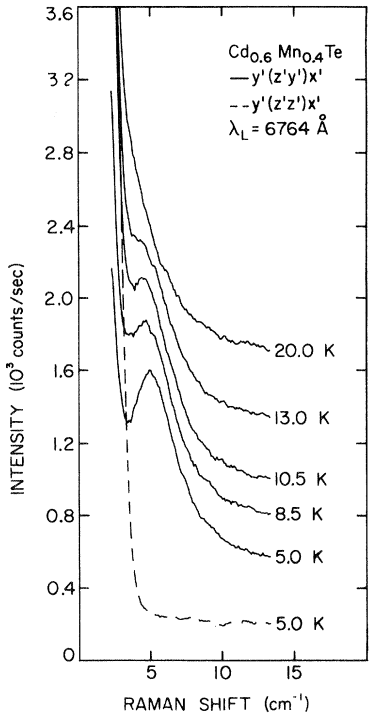

FIG. 14. Temperature dependence of the low-frequency Raman spectrum of $Cd_{0.6}Mn_{0.4}Te$ ($T_N \sim 13$ K). The intensity scale refers to the $y'(z'z')x'$ spectrum and successive spectra have been displaced vertically upwards for clarity. The respective sample temperature is indicated for each trace. The broken curve shows the $y'(z'z')x'$ polarization (*VV*). All the other spectra correspond to $y'(z'y')x'$ polarization (*VH*); x', y', and z' are along [100], [011], and [$0\bar{1}1$]. λ_L indicates the excitating laser wavelength.

other hand, even at 5 K, the line is completely quenched in the *VV* polarization as seen from the lowermost trace in Fig. 13. Thus, the observed polarization behavior as well as the temperature dependence of this line are consistent with those expected for one-magnon scattering. Very similar results were obtained for other alloys exhibiting the antiferromagnetic phase. For example, at 5 K the $x=0.65$ sample displays a magnon line at 10.5 cm^{-1}; the line disappears above $T_N \sim 33$ K and has antisymmetric polarization.

Well below T_N, we observed a distinct magnon line with antisymmetric polarization in the spin-glass phases of $x=0.4$ and 0.5 samples as well. At 5 K their magnon peak position was in the range 4.5–5.5 cm^{-1}. Typical results obtained for $x=0.4$ are shown in Fig. 14. Here the lowermost trace shows the spectrum in the $y'(z'z')x'$ polarization (*VV*) at 5 K, while the one immediately above corresponds to $y'(z'y')x'$ polarization (*VH*) at the same temperature; x', y', and z' are, respectively, along [100], [011], and [$0\bar{1}1$]. We note that for crystals of point group symmetry T_d, only modes of E symmetry or those belonging to the antisymmetric F_1 representation can appear in $y'(z'y')x'$ scattering configuration. On the other hand, in the $y'(z'z')x'$ geometry the E modes are allowed, but F_1 modes are forbidden.[10] This establishes that the line seen at 5 cm^{-1} at $T=5$ K indeed belongs to an antisymmetric representation. Its disappearance above $T_N \sim 13$ K further confirms that this line could originate from spin waves within the spin-glass phase.

The appearance of a magnon peak in the spin-glass phase may be related to the possible presence of antiferromagnetic grains of finite size. As Galazka *et al.* have noted,[7] the size and density of these grains are expected to be a function of x. We also anticipate that the frequency of the magnon line should decrease when x is lowered. This is a consequence of the reduced effective-exchange

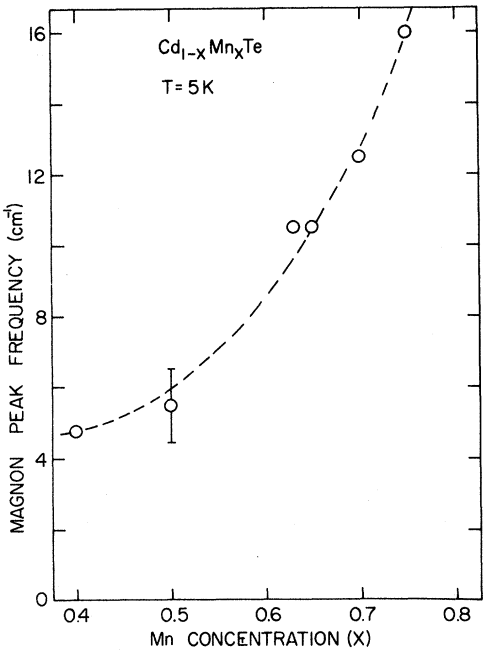

FIG. 15. Variation of the observed magnon-peak frequency with Mn concentration (x); $T=5$ K. Error bar indicates the typical accuracy of the spectrometer in measuring the peak position. The broken line is a smooth curve drawn through the data points.

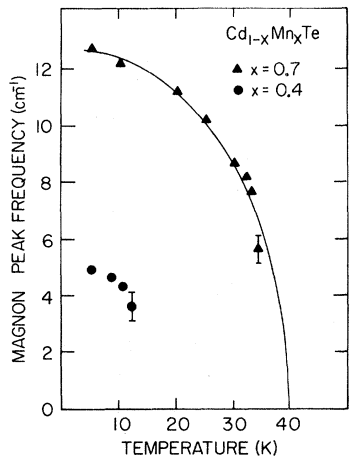

FIG. 16. Temperature dependence of the magnon-peak frequency in the magnetically ordered phases of $Cd_{1-x}Mn_xTe$. Triangles: $x=0.7$, antiferromagnetic phase; circles: $x=0.4$, spin-glass phase. The solid curve passing through the points for $x=0.7$ is calculated for $T_N=40$ K solving Eq. (20) for M_s as a function of $T \leq T_N$ and assuming ω_M is proportional to M_s and equal to 12.5 cm^{-1} at $T=0$ K.

field between adjacent Mn^{2+} moments. The experimental results shown in Fig. 15 are consistent with this expectation. With increasing dilution of the Mn^{2+} ions, we were unable to observe a distinct peak for $x<0.4$. The results obtained in the spin-glass phase for $x=0.3$ with $T_N \sim 7$ K show that even at 3.8 K, we could detect only a monotonically falling inelastic wing which extends to about 7 cm^{-1} away from the exciting laser line; as with the magnon peaks, this wing is seen only in the off-diagonal polarization.

Figure 16 shows the temperature dependence of the magnon peak for $x=0.7$ and 0.4. Ascribing the magnon peak to a single quantum excitation, a molecular-field theory can provide an interpretation based on the macroscopic parameters, H_A and $H_E=|\lambda\vec{M}_1|=|\lambda\vec{M}_2|$. The solution of the Bloch equations[42] gives the long-wavelength magnon frequency, $\omega_M=\gamma(H_A^2+2H_AH_E)^{1/2}$, where $\gamma=ge/2mc$ is the gyromagnetic ratio of Mn^{2+} having $S=\frac{5}{2}$ and hence, $g=2$. We assume that H_A like H_E is proportional to the saturation values of M_1 or M_2 given by

$$M_S=(2xg\mu_BS/a^3)B_S(y)\ , \tag{20}$$

where μ_B is the Bohr magneton, a the lattice constant, and $B_S(y)$ the Brillouin function with

$$y=\frac{g\mu_BS}{k_BT}(H_A+H_E)\equiv\frac{g\mu_BS}{k_BT}(\lambda+\mu)M_S\ .$$

The Néel temperature, T_N, is then given by

$$k_BT_N=(2x/3a^3)g^2\mu_B^2S(S+1)(\lambda+\mu)\ . \tag{21}$$

A numerical solution of Eq. (20) yields M_S as a function of temperature, T, and in turn the variation of ω_M with T. The best fit for our data shown in Fig. 16 for $x=0.7$ is given by $T_N=40$ K. This value is to be compared with $T_N=36\pm2$ K obtained by Galazka *et al.*,[7] from the maximum in the excess in the specific heat of the alloy over that of pure CdTe as well as from the discontinuity of the slope of the magnetic susceptibility as a function of T. From Eq. (21), using $a=6.39$ Å for $x=0.7$ (Giriat[43]) together with the peak position of the Raman line at the lowest temperature, we obtain $\lambda=872$ and $\mu=153$; these parameters yield $(J/k_B)=-(g^2\mu_B^2\lambda/Za^3k_B)=-2$ K. Here J is the exchange energy and Z, the effective number of antiparallel nearest neighbors. In calculating J we have assumed that in "MnTe" the Mn^{2+} spins on the fcc sublattice are oriented such that eight of the nearest-neighbor Mn^{2+} are antiparallel to the remaining four.[44] Using the experimental value for the magnetic susceptibility χ of Galazka *et al.*[7]

and recalling that

$$\chi=\tfrac{2}{3}\chi_{\perp}=(2g^2\mu_B^2/3Za^3\,|J|)\ ,$$

where $\chi_{\perp}$ is the magnetic susceptibility for an applied magnetic field perpendicular to $\vec{M}_1$ and $\vec{M}_2$ and $Z=4$, we obtain $J/k_B=-8.8$ K. We emphasize, however, that while our results on the temperature dependence of ω_M and the results of Galazka *et al.*[7] on the temperature dependence of the excess specific heat as well as of χ are in agreement, it is the smaller measured low-temperature value of χ which yields the larger value of J.

It is of interest to inquire whether the magnon peak arises from a two-magnon instead of a one-magnon scattering process. Following Buchanan *et al.*[45] the exchange constant J can be used[46] to evaluate the approximate peak position and width of the two-magnon scattering profile. The first and second moments of the normalized intensity profile $[I(\omega)]$ that are of interest here are given by

$$\langle\omega\rangle=\int I(\omega)\omega\,d\omega\ , \tag{22}$$

and

$$\langle(\Delta\omega)^2\rangle=\langle(\omega-\langle\omega\rangle)^2\rangle \tag{23}$$
$$=\int I(\omega)(\omega-\langle\omega\rangle)^2 d\omega\ .$$

If $I(\omega)$ is assumed to be approximately Gaussian with the full width at half maximum intensity being Γ, we have, in addition,

$$\Gamma^2=5.55\langle(\Delta\omega)^2\rangle\ . \tag{24}$$

The results of Buchanan *et al.*[45] lead to the following two equations:

$$\hbar\langle\omega\rangle=2Ax\ , \tag{25}$$

$$\hbar^2\langle(\omega-\langle\omega\rangle)^2\rangle=\frac{4}{Z}A^2x(1-x)\ , \tag{26}$$

with $A=2Z\,|J|\,S$. Equation (22) also yields the approximate peak frequency of $I(\omega)$. Equations (22)–(26) allow us to estimate $\langle\omega\rangle$ and Γ. With $|J|=2$ K, the two-magnon peaks, if present, will overlap with the intense phonon spectra in the range 17–40 cm^{-1}, as x varies from 0.3 to 0.7 and at even higher frequencies if J is larger. Furthermore, the estimated values of Γ indicate that the two-magnon scattering would be considerably diffuse and broadened.

Our spectra do not reveal any strong features in the expected frequency range of two-magnon scattering for all the alloys investigated. We therefore believe that the magnon peaks seen in Figs. 12–14 are due to one-magnon scattering. The completely antisymmetric polarization of these peaks also supports this view. Finally, the temperature dependence of the magnon peak position for $x=0.7$ and 0.4 shown in Fig. 16 reinforces this interpretation. In contrast, two-magnon peaks seen in other typical antiferromagnetic crystals,[47] such as NiF_2 or FeF_2 do not exhibit such a marked softening but persist at temperatures well above T_N.

It is of course plausible that the observed magnon profiles reflect the one-magnon density of states in view of the absence of strict translational symmetry. In such a case, the $\vec{q}\sim 0$ selection rule is relaxed and magnons with large $\vec{q}$ vectors can make a contribution to the observed intensity. Such excitations are determined mainly by the short-range interactions between the spins. These interactions persist above T_N, and highly damped spin-wave exitations with large $\vec{q}$ vector have been observed even in the paramagnetic phase.[47] From Figs. 13 and 14, we note that above T_N a clear inelastic wing is present in *VH* polarization but not in *VV*. This behavior was noticed over the concentration range $0.1\le x\le 0.75$. Such an antisymmetric wing is consistent with the magnetic excitations with residual clusters of antiferromagnetically coupled Mn^{2+} spins within the paramagnetic phase. In fact, model calculations performed by Nagata *et al.*[48] indicate that in clusters containing several Mn^{2+} spins, a quasicontinuum of energy levels is to be expected. We therefore attribute the antisymmetric wing observed in the paramagnetic phase to transitions involving such a continuum.

ACKNOWLEDGMENTS

We wish to thank Professor J. K. Furdyna and Professor P. H. Keesom for stimulating our interest in these mixed crystals and for valuable discussions. We also express our appreciation to Professor W. Gebhardt for helpful discussions concerning the two-magnon Raman spectra of $Cd_{1-x}Mn_xTe$ and to Dr. A. J. Strauss and Dr. W. Giriat for providing some of the samples used in this investigation. The work was supported in part by the NSF-MRL Program No. DMR 77-23798 and the National Science Foundation Grant No. DMR 77-27248.

*Present address: Department of Physics, State University of New York, Binghamton, N.Y. 13901.
†Present address: Institute of Physics, Polish Academy of Sciences, Warsaw, Poland.

[1]D. Long and J. L. Schmit, *Semiconductors and Semimetals,* edited by R. K. Willardson and A. C. Beer (Academic, New York, 1970), Vol. 5, p. 175.
[2]R. R. Galazka, in *Physics of Semiconductors 1978,* edited by B. L. H. Wilson (The Institute of Physics, Bristol, 1979), p. 133.
[3]G. Bastard, C. Rigaux, Y. Guldner, J. Mycielski, and A. Mycielski, J. Phys. (Paris) 39, 87 (1978).
[4]J. A. Gaj, J. Ginter, and R. R. Galazka, Phys. Status Solidi B 89, 655 (1978).
[5]J. A. Gaj, R. R. Galazka, and M. Nawrocki, Solid State Commun. 25, 193 (1978).
[6]M. Jaczynski, J. Kossut, and R. R. Galazka, Phys. Status Solidi B 88, 73 (1978).
[7]R. R. Galazka, S. Nagata, and P. H. Keesom, Phys. Rev. B 22, 3344 (1980).
[8]A. S. Barker and A. J. Sievers, Rev. Mod. Phys. 47, Suppl. 2 (1975).
[9]N. T. Khoi and J. A. Gaj, Phys. Status Solidi B 83, K133 (1977).
[10]Brief reports have appeared in: S. Venugopalan, A. Petrou, R. R. Galazka, and A. K. Ramdas, Solid State Commun. 38, 365 (1981); 35, 401 (1980). See also *Proceedings of the Seventh International Conference on Raman Spectroscopy,* edited by W. F. Murphy (North-Holland, Amsterdam, 1980), p. 78.
[11]Although the Laue pictures of some of the samples showed uniaxial symmetry, we noticed that the corresponding x-ray powder diffraction patterns always displayed cubic symmetry. Based on our observations, the possible occurrence of twinning effects was brought to our attention by Dr. A. Y. Wu (private communication).
[12]The polishing accessories were supplied by: Buehler Ltd., 2120 Greenwood St., Evanston, IL 60204.
[13]W. Imaino, C. T. Simpson, W. M. Becker, and A. K. Ramdas, Phys. Rev. B 21, 634 (1980).
[14]"Super Varitemp" Model 10DT, Janis Research Co., 22 Spencer St. Stoneham, MA 02187.
[15]Model DTC 500-SP, Lakeshore Cryotronics, Inc., 64 E. Walnut St., Westerville, OH 43081.
[16]Syton HT-30. Manufactured by Monsanto and distributed by Remet Chemical Corporation, Box 278, Chadwicks, NY 13319.
[17]W. Hayes and R. Loudon, *Scattering of Light by Crystals* (Wiley, New York, 1978), pp. 44–46.
[18]A. Mooradian and G. B. Wright, *Proceedings of the Ninth International Conference on the Physics of Semiconductors, Moscow,* edited by S. M. Ryvkin (Nauka, Leningrad, 1968), p. 1020.
[19]M. Selders, E. Y. Chen, and R. K. Chang, Solid State Commun. 12, 1057 (1973).
[20]I. Nair and C. T. Walker, Phys. Rev. B 3, 3446 (1971).
[21]R. T. Harley, J. B. Page, and C. T. Walker, Phys. Rev. B 3, 1365 (1971).
[22]The zinc-blende structure is hypothetical for MnTe, as pure MnTe crystallizes in the hexagonal nickel-arsenide structure which has C_{6v}^4 symmetry.
[23]M. Picquart, E. Amzallag, M. Balkanski, C. Julien, W. Gebicki, and W. Nazarewicz, Phys. Status Solidi B 99, 683 (1980).
[24]W. Gebicki and W. Nazarewicz, Phys. Status Solidi B 86, K135 (1978).
[25]See, for example I. M. Lifshitz and A. M. Kosevich, Rep. Prog. Phys. 29, Part I, 217 (1966).
[26]A. A. Maradudin and J. Oitmaa, Solid State Commun. 7, 1143 (1969).
[27]H. Fröhlich, *Theory of Dielectrics* (Oxford, London, 1958).
[28]Here $n^2=\epsilon_\infty$, the high-frequency dielectric constant is calculated from the static dielectric constant, $\epsilon_0=9.6$ [D. Berlincourt, H. Jaffe, and L. R. Shiozawa, Phys. Rev. 129, 1009 (1963)], the Raman frequencies of ω_{LO} and ω_{TO} (Ref. 18), and the Lydanne-Sachs-Teller relation. The value for z, the charge on Mn^{2+} is assumed to be 2. The lattice parameter has been determined by W. D. Lawson, S. Nielsen, and A. S. Young, in Proceedings of the International Conference on Solid State Phys. Electron. Telecommun., 1960, Vol. 2, p. 830. See also K. Zanio, *Semiconductors and Semimetals,* edited by R. K. Willardson and A. C. Beer (Academic, New York, 1978), Vol. 13, p. 53.
[29]E. Jahne, Phys. Status Solidi B 74, 275 (1976); 75, 221 (1976).
[30]L. Genzel, T. P. Martin, and C. H. Perry, Phys. Status Solidi B 62, 83 (1974).
[31]D. N. Talwar, M. Vandevyver, and M. Zigone, J. Phys. C 13, 3775 (1980).
[32]C. T. Sennett, D. R. Bosomworth, W. Hayes, and A. R. L. Spray, J. Phys. C 2, 1137 (1969). The frequency-dependent weighting factor $1/\omega^2$, however, is unimportant for our purposes; it is a model-dependent factor employed by Sennett *et al.*, for calculating the relative intensity of the sideband structure of a local mode. In view of this, the inset in Fig. 3(a) tends to de-emphasize the higher-frequency structure of $S(\omega)$, especially in the region of the optical modes.
[33]J. M. Rowe, R. M. Nicklow, D. L. Price, and K. Zanio, Phys. Rev. B 10, 671 (1974).
[34]See, for example, D. L. Rousseau and S. P. S. Porto, Phys. Rev. Lett. 20, 1354 (1968).
[35]S. Nakashima, T. Fukumoto, A. Mitsuishi, and K. Itoh, J. Phys. Soc. Jpn. 35, 1437 (1973).
[36]R. M. Martin and L. M. Falicov, *Light Scattering in Solids,* edited by M. Cardona (Springer, Berlin, 1975), p. 79.
[37]W. Richter, in *Solid State Physics,* Vol. 78 of *Springer Tracts in Modern Physics,* edited by K. Seeger (Springer, Berlin, 1976), p. 121.
[38]R. Trommer, G. Abstreiter, and M. Cardona, in *Lattice Dynamics,* edited by M. Balkanski (Flammarion

Sciences, Paris, 1977), p. 189.
[39]L. D. Landau and E. M. Lifshitz, *Electrodynamics of Continuous Media* (Pergamon, Oxford, 1960), p. 331. See also Ref. 17, p. 240.
[40]P. A. Fleury and R. Loudon, Phys Rev. 166, 514 (1968).
[41]T. R. Hart, R. L. Aggarwal, and B. Lax, in *Light Scattering in Solids,* edited by M. Balkanski (Flammarion Sciences, Paris, 1971) p. 174.
[42]C. Kittel, *Introduction to Solid State Physics,* 5th ed. (Wiley, New York, 1976).
[43]W. Giriat (private communication).
[44]T. Giebultowicz, H. Kepa, B. Buras, K. Klausen, and R. R. Galazka, Solid State Commun. 40, 499 (1980).
[45]M. Buchanan, W. J. L. Buyers, R. J. Elliott, R. T. Harley, W. Hayes, A. M. Perry, and I. D. Saville, J. Phys. C 5, 2011 (1972).
[46]W. Gebhardt (private communication).
[47]P. A. Fleury, Phys. Rev. 180, 591 (1969).
[48]S. Nagata, R. R. Galazka, D. P. Mullin, H. Akbarzadeh, G. D. Khattak, J. K. Furdyna, and P. H. Keesom, Phys. Rev. B 22, 3331 (1980).